Available online at www.sciencedirect.com

ScienceDirect

Progress in Natural Science: Materials International 24 (2014) 266–273

Progress in Natural Science Materials International

www.elsevier.com/locate/pnsmi
www.sciencedirect.com

Original Research

# Microstructure heterogeneity and creep damage of DZ125 nickel-based superalloy

Haofang Sun[a], Sugui Tian[a,*], Ning Tian[a], Huichen Yu[b], Xianlin Meng[a]

[a]School of Materials Science and Engineering, Shenyang University of Technology, Shenyang 110870, China
[b]Beijing Institute of Aeronautical Materials, Beijing 100095, China

Received 5 April 2014; accepted 27 April 2014
Available online 28 May 2014

**Abstract**

The creep behavior of the DZ125 superalloy at high temperatures has been investigated based on the creep properties measurement and microstructure observations. The experimental results show that, after full heat treatment, the fine and coarser cuboidal $\gamma'$ precipitates distributed in the dendrite arm and inter-dendrite regions, respectively, the boundaries with various configurations located in the inter-dendrite regions. In the primary creep stage, the cuboidal $\gamma'$ phase in the alloy transformed into the rafted structure along the direction vertical to the stress axis. The dislocations slipping and climbing over the rafted $\gamma'$ phase are attributed the deformation mechanism of the alloy during steady-state creep. The $(1/2)\langle 1\ 1\ 0\rangle$ dislocations slipping in the $\gamma$ matrix and $\langle 1\ 1\ 0\rangle$ super-dislocations shearing into the $\gamma'$ phase are the deformation mechanisms of the alloy in the latter stage of creep. And then the alternate slipping of dislocations results in the initiation and propagation of the micro-cracks along the boundaries until the occurrence of the creep fracture. Since the grain boundaries with various angles relative to the stress axis distribute in the different regions, the initiation and propagation of micro-cracks along the boundaries display the various features.


*Keywords:* DZ125 nickel-based superalloy; Microstructure; Creep mechanism

## 1. Introduction

The microstructure of directional solidification (DS) nickel-based superalloys mainly consists of $\gamma$ matrix and $\gamma'$ phases. For columnar-crystal structure formed along the $\langle 0\ 0\ 1\rangle$ direction in the alloys during solidification, the horizontal grain boundaries perpendicular to the stress axis are eliminated [1,2]. Compared to common poly-crystal casting alloys, the DS alloys have the better creep resistance, and therefore have been widely used for making the blade parts in advanced aero-plane engines [3,4].

Despite the horizontal boundaries of DS nickel-base superalloys being eliminated, the creep damage is still the main failure model for them during the service, including the coarsening of the $\gamma'$ phase, dislocations slipping in matrix and shearing $\gamma'$ phase, and the formation of micro-cracks in the interface of $\gamma/\gamma'$ phases [5]. As the dislocation-moving model and the crack-initiating and -propagating models are closely related to the creep resistance of the alloys during creep at high temperature, it is very important to study the creep behavior of DS alloys.

Previous studies have indicated that the nickel-based single crystal superalloys possess various deformation features at different stages of creep at high temperature [6–8], dislocations sliding in the $\gamma$ matrix are the main deformation feature in the primary stage of creep. During the steady state creep the $\gamma'$ phase in alloy transforms into the rafted structure along the

*Corresponding author. Tel.: +86 24 25494089.
*E-mail address:* tiansugui2003@163.com (S. Tian).
Peer review under responsibility of Chinese Materials Research Society.

Production and hosting by Elsevier

http://dx.doi.org/10.1016/j.pnsc.2014.05.004

direction vertical to the stress axis, and the dislocation networks distribute in the interface of the $\gamma'/\gamma$ phases [9]. Also, the dislocations slipping in the $\gamma$ matrix and climbing over the rafted $\gamma'$ phase are considered as the deformation mechanism of alloys during steady-state creep [10]. In the latter stage of creep, the deformation mechanism of the alloy is dislocations moving in the matrix channels and shearing into the $\gamma'$ phase [11,12].

DZ125 alloy is one of the DS casting alloys [13,14] possessing better mechanical and creep properties at high temperatures, and excellent thermal fatigue properties. As the casting temperature increases, the dislocation density in the as-cast alloy increases and the dislocations distribute in the form of the wavy-like and network-like morphology [15,16]. In particular, some Hf atoms are distributed in the boundary regions of the DZ125 alloy, which causes the carbides and borides to be dispersedly precipitated along the boundaries. These can delay and restrain the initiation and propagation of cracks along the boundaries to improve the creep resistance of the alloy [17]. Despite the microstructure and creep properties of DS superalloys having been extensively researched, a few studies have reported the creep behavior of the DZ125 superalloy during creep at high temperature, while the deformation mechanisms and damage model of the alloy during creep remains unclear.

Hereby, by means of creep property measurement and microstructure observation, the deformation mechanisms and damage behavior of the DZ125 alloy during creep at high temperatures are investigated.

## 2. Experimental procedures

The bars of DZ125 nickel-based superalloy with [0 0 1] orientation were prepared in a vacuum directional solidification furnace. The nominal chemical compositions of the alloy are shown in Table 1. The heat-treatment of the bars was: 1180 °C, 2 h+1230 °C, 3 h, AC+1100 °C, 4 h, AC+870 °C, 20 h, AC. After being fully heat treated, the bars of the alloy were cut into a plate-like creep specimen with cross-section of 4.5 mm × 2.5 mm and gauge length of 15.0 mm.

After grinding and polishing the specimen was put into a GWT504 model creep-testing machine and uniaxial constant load tensile tests were performed, under the different conditions, to measure the creep properties of the alloy. In addition, the creep tests were interrupted at different times to observe the microstructures of the alloy by scanning electron microscopy (SEM) and transmission electron microscopy (TEM) to investigate the creep behavior and deformation mechanism of the DZ125 nickel-based superalloy.

Table 1
Chemical compositions of DZ125 superalloy (mass fraction, %).

| Cr | Co | W | Mo | Al | Ti | Ta | Hf | B | C | Ni |
|---|---|---|---|---|---|---|---|---|---|---|
| 8.68 | 9.80 | 7.08 | 2.12 | 5.24 | 0.94 | 3.68 | 1.52 | 0.012 | 0.09 | Bal. |

## 3. Experimental results and analysis

### 3.1. Microstructures of alloy

After being fully heat treated, the integrated dendrite morphology still remains on the (1 0 0) plane of the alloy, as shown in Fig. 1(a), where the long line represents the growing direction of the primary dendrite and the short line represents the growing direction of the secondary dendrite, which is vertical to the primary one.

The magnified morphology in the local region on the (1 0 0) plane is shown in Fig. 1(b), indicating that the microstructure of the alloy consists of the cuboidal $\gamma'$ phase embedded coherently in the $\gamma$ matrix. The fine cuboidal $\gamma'$ phase dispersedly distributed in the dendrite arm regions, and the coarser cuboidal $\gamma'$ phase distributed in the inter-dendrite regions. Due to the mis-orientation between the dendrites the boundaries existed in the inter-dendrite regions, as marked by the white arrow. The amplification morphology of the region A is shown in Fig. 1(c), indicating that the fine $\gamma'$ precipitates dispersedly distributed in the dendrite regions, and the average size of the cuboidal $\gamma'$ phase is about 0.4 μm. However, the coarser cuboidal $\gamma'$ phase distributed in the inter-dendrite region B, where the smaller cuboidal $\gamma'$ phase is about 0.7 μm in size, as marked by the short arrow in Fig. 1(d), while some coarser cuboidal $\gamma'$ precipitates are about 1.5 μm in size, as marked by the long arrow. This indicates that the inhomogeneous cuboidal $\gamma'$ phase in size distributed in the area between the dendrite and inter-dendrite regions.

### 3.2. Creep behavior of alloy

The creep curves of the alloy under different conditions are measured, as shown in Fig. 2. Fig. 2(a) shows the creep curves of the alloy under the applied different stresses at 1040 °C, indicating that the alloy displays various creep features at different conditions. It is indicated that the small strain and short lasting time occurs in the primary stage of creep, which corresponds to significant amount of dislocations activated in the $\gamma$ matrix [18]. As the creep goes on the density of dislocations increases, which will decrease the strain rate of alloy due to the effect of the strain strengthening, and then the creep of alloy enters the steady-state stage. Under the applied stresses of 127 MPa, the strain rate of the alloy during steady-state creep was measured to be 0.0183%/h and the creep life was 109 h, as shown by curve 1 in Fig. 2(a). In addition, as the applied stress increased to 137 MPa, the strain rate of the alloy during steady-state creep enhanced to 0.0238%/h and the creep life decreased to 90 h, as shown by curve 2 in Fig. 2(a). As the applied stress further enhanced to 147 MPa, the strain rate of the alloy during steady-state creep increased to 0.0313%/h, and the creep life further decreased to 49.5 h, as shown in the curve 3 of Fig. 2(a). In particular, the creep life of the alloy at 1040 °C decreased from 90 h to 49.5 h, with the 82% decrement of the creep life, when the applied stress increased from 137 MPa to 147 MPa. This indicates that the creep feature of

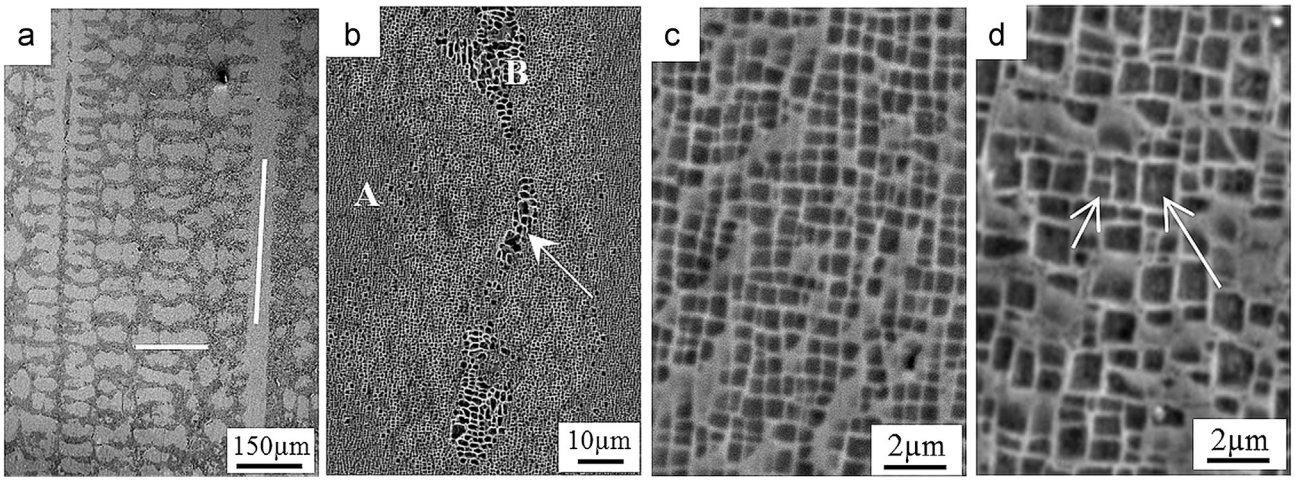


Fig. 1. Microstructure in the different regions of the alloy after full heat treatment. (a) Dendrite morphology on (1 0 0) plane, (b) magnified morphology in the dendrite/inter-dendrite regions, (c) fine $\gamma'$ phase in the dendrite region, (d) coarser $\gamma'$ phase in the inter-dendrite region.

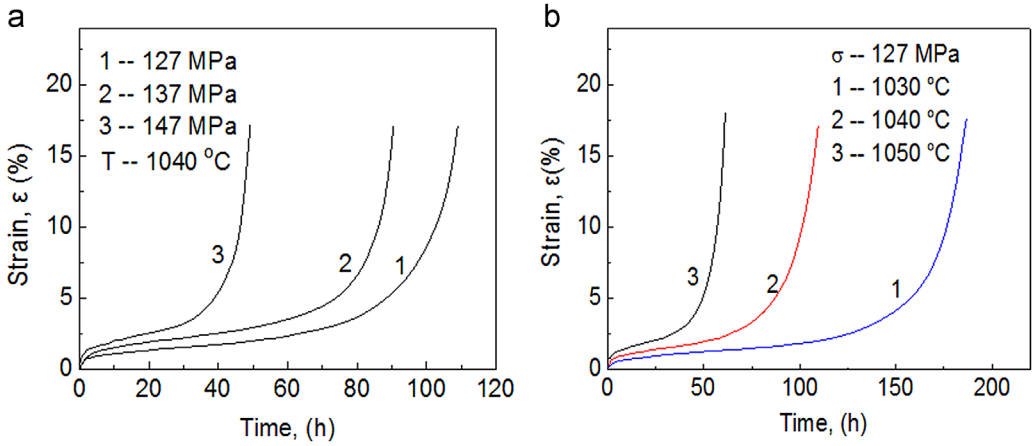


Fig. 2. Creep curves of alloy under different conditions. (a) Applied different stresses at 1040 °C, (b) applied stress of 127 MPa at different temperatures.

the alloy at 1040 °C displays an obvious sensibility to the applied stress when the applied stress was higher than 137 MPa.

The creep curves of the alloy under the applied stress of 127 MPa at different temperatures are shown in Fig. 2(b), in which the strain rates of the alloy during steady-state creep at 1030 °C was measured to be 0.0146%/h, and the creep life was 186 h, as marked by the curve 1 in Fig. 2(b). As the creep temperature enhanced to 1040 °C, the creep life of the alloy was 90 h. As the creep temperature enhanced further to 1050 °C, the strain rate of the alloy increased to 0.02334%/h, and the creep life of the alloy decreased to 61 h, as marked by the curve 3 in Fig. 2(b).

The transient strain of the alloy occurs at the moment of applying load at high temperatures. And the density of dislocations in the alloy increases as creep goes on, which results in the strain hardening to decrease the strain rate of the alloy [19]. The strain rate of the alloy maintains constant when the creep of the alloy enters the steady-state stage. Also, the strain rate of the alloy during steady-state creep can be expressed by Dorn law given as follows [20]:

$$\dot{\varepsilon}_{ss} = A\sigma_A^n \exp\left(-\frac{Q}{RT}\right) \quad (1)$$

Here, $\dot{\varepsilon}_{ss}$ is the strain rate during steady-state creep, $A$ is a constant related to material structure, $\sigma_A$ is the applied stress, $n$ is the apparent stress exponent, $R$ is the gas constant, $T$ is thermodynamics temperature, $Q$ is the apparent creep activation energy.

Based on the measurement of the strain rates of the alloy under different conditions, as shown in Fig. 2, the dependence of the strain rate of the alloy on the applied stresses and temperatures was plotted, as shown in Fig. 3(a) and (b), respectively. Furthermore, in the temperature range of 1030–1050 °C and stress range of 127–147 MPa, the apparent creep activation energy and apparent stress exponent of the DZ125 superalloy were calculated to be $Q = 338.42$ kJ/mol and $n = 3.7$, respectively.

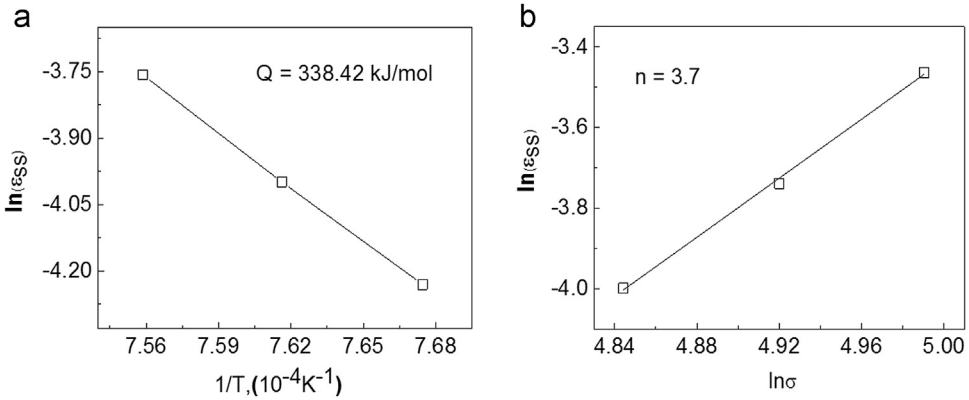


Fig. 3. Relationship between the strain rates of the alloy during steady state creep and applied temperatures, stresses. (a) Strain rates and temperature, (b) strain rates and applied stress.

According to the data in Fig. 3 it is indicated that the DZ125 nickel-based superalloy has a higher apparent creep activation energy, suggesting that the alloy has the good creep resistance in the applied stress range of 127–147 MPa and temperature range of 1030–1050 °C, which is in agreement with the results in Fig. 2. Also, it can be deducted according to the calculating stress exponent that the dislocation slipping within the $\gamma$ matrix and climbing over the rafted $\gamma'$ phase could be the main deformation mechanisms of the alloy during steady-state creep in the ranges of the applied stress and temperature in the present investigation.

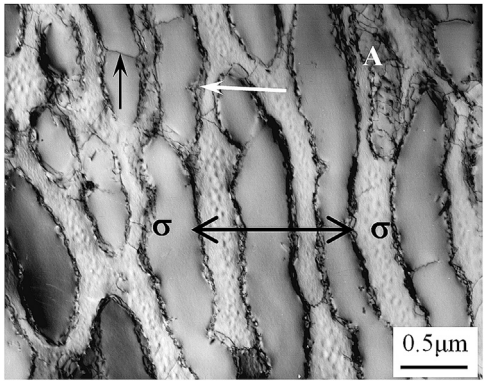


Fig. 4. Microstructure of the alloy crept for 40 h during steady state creep.

### 3.3. Deformation features during creep

The microstructure of alloy after creeping for 40 h at 1040 °C/137 MPa is shown in Fig. 4, indicating that the $\gamma'$ phase in the alloy has transformed into the rafted structure along the direction perpendicular to the stress axis when the creep of the alloy entered the steady-state stage, and the direction of the applied stress is marked by the arrows in Fig. 4. It is indicated from Fig. 4 that some dislocation networks distributed in the interfaces of the rafted $\gamma/\gamma'$ phases, as marked by the longer arrow, and a few dislocation sheared into the rafted $\gamma'$ phase, as marked by the short arrow.

Fig. 4 also demonstrates that the denser dislocations were moving in the $\gamma$ matrix channels, as marked in the region A, the moving dislocations might react each other to form dislocation networks [21] and distributed in the interfaces of the $\gamma'/\gamma$ phases. Moreover, it is believed that after the creep dislocations in the $\gamma$ matrix channels moved to the interfaces of the $\gamma'/\gamma$ phases, the ones might react with the dislocation networks, and hence the resolved segments changed the original moving direction to promote the dislocations climbing to another slipping plane [16], which may relieve the stress concentration of the alloy during creep. Therefore, it can be deduced that the dislocation networks have an important coordinating action on the strain hardening and recovery softening of the alloy during steady-state creep. Furthermore, the fact that few dislocations sheared into the rafted $\gamma'$ phase indicates that the deformation mechanism of the alloy during steady-state creep is the dislocations climbing over the rafted $\gamma'$ phase.

The microstructure of the specimen creep tested for 90 h up to fracture under the test condition of 137 MPa/1040 °C is shown in Fig. 5. The microstructure far from the fracture is shown in Fig. 5(a), indicating that the N-type rafted structure still kept in the alloy; the direction of the applied stress is marked by the arrows in Fig. 5(a). However, the rafted $\gamma'$ phase in the alloy was twisted, and the size of the one in thickness increased slightly to about 0.6 μm. A significant amount of interface dislocations distributed in the interfaces of the $\gamma'/\gamma$ phases, and some dislocations had sheared into the rafted $\gamma'$ phase, as marked by the black arrow.

After crept up to fracture, the microstructure of the alloy in the region near fracture is shown in Fig. 5(b), indicating that interfacial dislocation networks in the local regions of the alloy were damaged due to the bigger plastic deformation in these regions. This results in a large number of dislocations shearing into the rafted $\gamma'$ phase to increase the strain value of the alloy. In the latter stage of creep, the fact that a large amount of dislocations sheared into the rafted $\gamma'$ phase indicates that the alloy had lost creep resistance. And it is considered that the deformation mechanism of alloy in the latter period of creep is the alternate activation of the primary/secondary slipping systems [22]. The primary slipping system was firstly activated to twist the rafted $\gamma'/\gamma$ phases, as marked by the letter B in

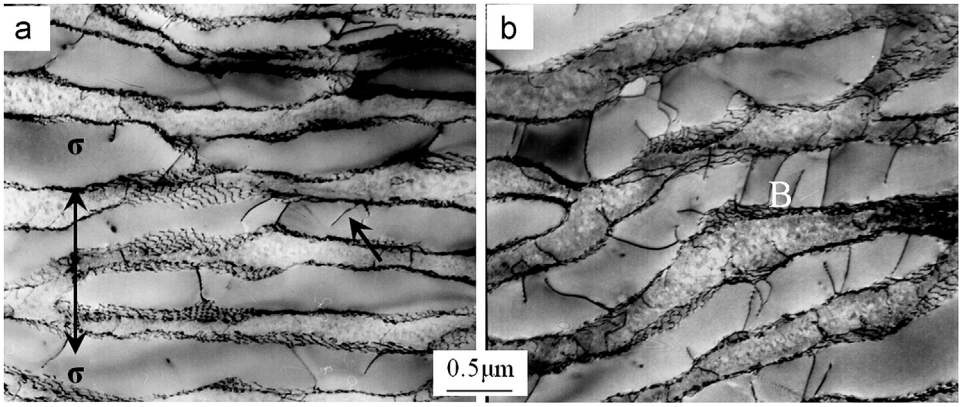


Fig. 5. Microstructure of alloy after being crept for 90 h up to fracture at 1040 °C/137 MPa, (a) twisted of the rafted $\gamma'$ phase, (b) alternate slipping of dislocations.

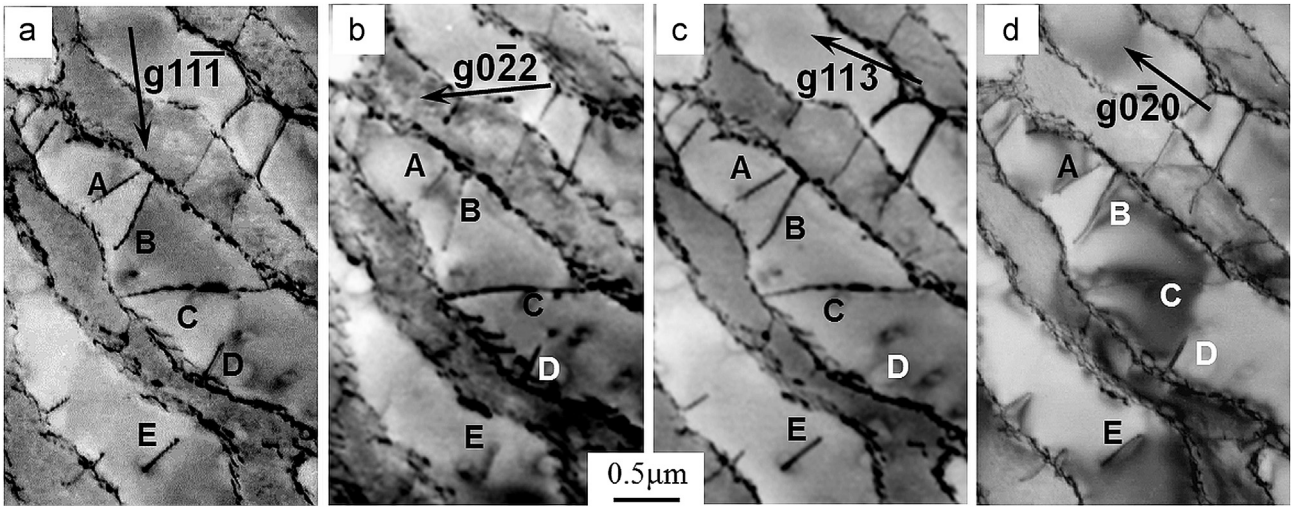


Fig. 6. Dislocation configuration within the rafted $\gamma'$ phase after the alloy crept for 90 h up to fracture at 1040 °C/137 MPa. (a) $\mathbf{g}=1\ \bar{1}\ \bar{1}$, (b) $\mathbf{g}=0\ \bar{2}\ 2$, (c) $\mathbf{g}=1\ 1\ 3$, (d) $\mathbf{g}=0\ \bar{2}\ 0$.

Fig. 5(b). And then the secondary slipping system was activated to shear the primary slipping system, which may promote the formation of some cavities along the intersected region of the primary/secondary slipping systems [23]. As the creep continues, the initiation of the micro-crack occurs in the interface of the $\gamma'/\gamma$ phases [24] to increase the strain of the alloy.

After the alloy was creep tested for 90 h up to facture at 1040 °C/137 MPa, the dislocation configuration within the rafted $\gamma'$ phase is shown in Fig. 6, where the configurations of dislocations shearing into the rafted $\gamma'$ phase are marked by the letters of **A, B, C, D** and **E**. It may be understood according to contrast analysis that the dislocation **A, B** and **E** display a weaker contrast when the diffraction vector is $\mathbf{g}=0\ \bar{2}\ 2$, as shown in Fig. 6(b). When the diffraction vectors were $\mathbf{g}=1\ \bar{1}\ \bar{1}$, $\mathbf{g}=1\ 1\ 3$ and $\mathbf{g}=0\ \bar{2}\ 0$, the dislocations **A, B** and **E** displayed contrast, as shown in Fig. 6(a), (c) and (d). Therefore, it can be determined according to the criteria of the dislocation invisible $\mathbf{b}\times\mathbf{g}=0$ that the dislocation **A, B** and **E** is the super-dislocation with Burgers vector $\mathbf{b}_A=\mathbf{b}_B=\mathbf{b}_E=[0\ 1\ 1]$.

When the diffraction vectors was $\mathbf{g}=0\ \bar{2}\ 0$, the dislocation **C** disappeared contrast, as shown in Fig. 6(d), and the one displays contrast when the diffraction vectors were $\mathbf{g}=1\ \bar{1}\ \bar{1}$, $\mathbf{g}=0\bar{2}2$ and $\mathbf{g}=1\ 1\ 3$, as shown in Fig. 6(a)–(c). Therefore, the dislocation **C** is identified as the super-dislocation with Burgers vector $\mathbf{b}_C=[1\ 0\ \bar{1}]$ according to the criteria of the dislocation invisible $\mathbf{b}\times\mathbf{g}=0$. Since the line vector of dislocation **C** is $\boldsymbol{\mu}_C=0\ \bar{2}\ 2$, the slipping plane of the dislocation **C** is identified as $\mathbf{b}_D\times\boldsymbol{\mu}_D=(1\ 1\ 1)$ plane.

When the diffraction vectors was $\mathbf{g}=1\ 1\ 3$, the dislocation **D** disappeared contrast, as shown in Fig. 6(c), and the one appeared contrast when the diffraction vectors were $\mathbf{g}=1\ \bar{1}\ \bar{1}$, $\mathbf{g}=0\ \bar{2}\ 2$ and $\mathbf{g}=0\ \bar{2}\ 0$, as shown in Fig. 6(a), (b) and (d). Therefore, the dislocation **D** is identified as the super-dislocation with Burgers vector $\mathbf{b}_D=[1\ \bar{1}\ 0]$ according to the criteria of the dislocation invisible $\mathbf{b}\times\mathbf{g}=0$. Because the line vector of dislocation **D** was $\boldsymbol{\mu}_D=2\ 0\ \bar{2}$, the slipping plane of the dislocation **D** is identified as $\mathbf{b}_D\times\boldsymbol{\mu}_D=$ (1 1 1) plane.

### 3.4. Initiation and propagation of cracks during creep

Fig. 7 shows surface morphology of the crack initiated and propagated along the boundaries of alloy after the specimens crept for different periods under the test condition of 1040 °C/137 MPa,

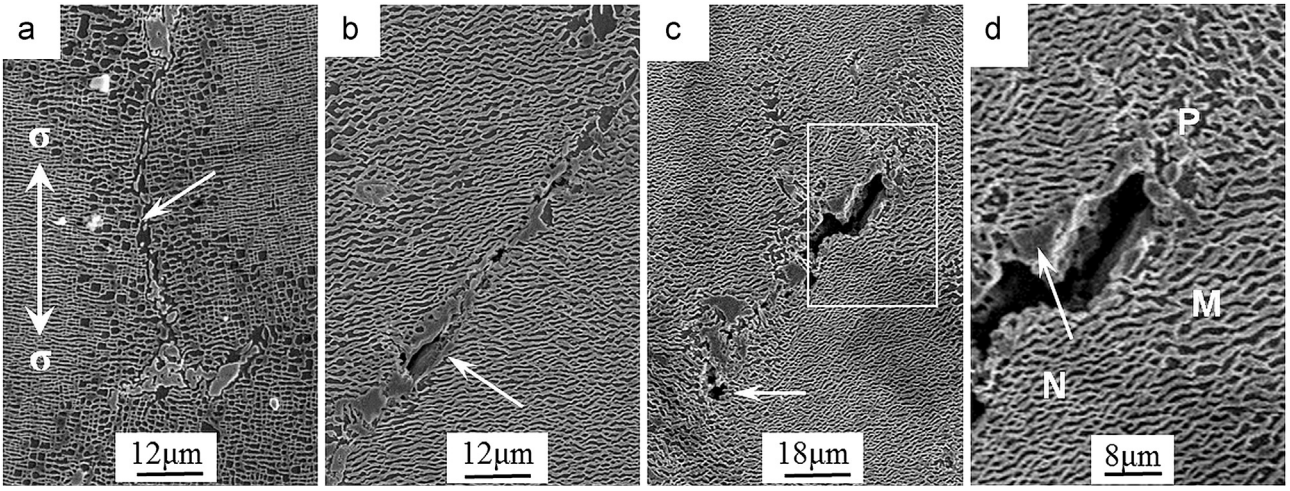


Fig. 7. Surface morphology of the specimens crept at 1040 °C/137 MPa: (a) upright boundary, (b) inclined boundary after crept for 75 h, (c) crack propagated along inclined boundary crept for 90 h, (d) magnified morphology of crack propagation.

and the direction of the applied stress is marked by the arrows in Fig. 7(a).

According to the results shown in Fig. 2, after the specimen was crept for 75 h, the creep of the alloy entered the accelerated creep stage, It is believed that when the dislocations slipping to the boundaries are hindered for piling up in the region near the boundaries, the stress concentration may be caused in the region. Once the value of stress concentration exceeds the bonding strength of the boundary, the initiation of cracks occurs firstly in the boundary region. But the grain boundaries in the alloy possess the different configurations, such as the boundaries are both parallel to the stress axis and about at 45° angles relative to the stress axis, therefore, the various deformation and damage of the specimen generated in the boundary regions with different configurations.

Fig. 7(a) and (b) shows the microstructure of the specimen crept for 75 h. It can be observed that although the creep of the specimen entered the accelerated stage, no the micro-crack was detected in the region of the boundary parallel to the stress axis, as shown in Fig. 7(a), in which the upright boundary is marked by the arrow. It is indicated from Fig. 7(a) that some particle-like carbides precipitated along the boundary, the coarser $\gamma'$ precipitates distributed in the regions near the boundary. But the initiation of the crack occurred along the boundary which is about at 45° angles relative to the stress axis, as marked by the white arrow in Fig. 7(b).

For the specimen crept for 90 h up to fracture, the morphology of the initiation and propagation of the micro-cracks along the boundaries is shown in Fig. 7(c), which indicates that the orientation of the boundary is about at 45° angles relative to the stress axis. The morphology of the crack initiating along the boundary is marked by the arrow in Fig. 7(c), the morphology of the crack propagating along the boundary is marked in the square frame region of Fig. 7(c), and the crack displays a Z-like feature. The magnified morphology in the square frame region is shown in Fig. 7(d). From Fig. 7(d) it can be observed that the inhomogeneous rafted $\gamma'$ phase in size distributed in the region near the boundary, the coarser rafted $\gamma'$ phase with twisted configurations distributed in the region M, while the fine rafted $\gamma'$ phase distributed in the region N. Moreover, the rafted $\gamma'$ phase with twisted and irregular configurations displayed in the region near the crack tip, indicating that compared to the $\gamma$ matrix phase, the rafted $\gamma'$ phase in the boundary region near the crack tip possesses a weaker strength, and therefore, the initiation of cracks occurred firstly in the grain boundaries.

The morphology of crack propagation of the crept specimen is shown in Fig. 7(d). It has been found that the particle-like carbide distributes in the edge of the crack, as marked by the arrow, and the surface of the fracture in the alloy displayed a non-smooth feature. Therefore, it may be thought by analysis that the particle-like carbide hindered the propagation of the crack. When the propagation of the crack was stopped by the particle-like carbide, the propagating direction of the crack changed to another orientation along the edge of the carbide, resulting in the Z-like configuration of the crack due to the pinning effect of the particle-like carbide, so that the fracture displays a non-smooth surface after the alloy is crept up to rupture.

In addition, during creep under the applied constant loading at high temperature, the bigger shearing stress occurs along the direction about at 45° angles relative to the stress axis. The bigger shear stress promotes significant amount of dislocations slipping along the direction at 45° angles relative to the stress axis, which may cause the stress concentration to promote the initiation and propagation of the cracks [25] along the boundary at 45° angles relative to the stress axis. Based on the analysis it is considered that some cavities and micro-cracks appear along the boundaries in the latter stage of creep, and the adjacent cavities or micro-cracks along the boundary are congregated as the creep continues, which results in the propagation of the crack along the boundaries to promote the occurrence of creep fracture as the propagation of the cracks in the other regions.

The microstructure observation indicates that the damage of the alloy during creep occurs firstly in the boundary regions, and the fracture of the alloy displays an unsmooth feature after the initiation and propagation of cracks occur along boundaries up to fracture, which suggests a high resistance for the propagation of cracks. It is believed that adding element Hf has an obvious role on improving the bonding force and slipping resistance of boundaries due to the Hf atom segregation in the boundaries to promote the precipitation of fine carbides and borides. The dispersed distribution of fine carbides along the boundaries has a pinning effect, which may restrain the slipping of the grain boundaries, and hence improve the creep resistance of the alloy.

## 4. Discussion

### 4.1. Resistance to dislocation motion

Compared to the $\gamma'$ phase, the $\gamma$ matrix phase possesses a lower strength, therefore the creep resistance of the alloy is related to the alloying degree of the refractory elements in the $\gamma$ phases. The creep resistance of the alloy increases with the content of the refractory elements. The dependence of the creep resistance of the alloy on the content of the refractory elements is expressed as following equation of [26].

$$\sigma_{ss} = AC^{1/2} \tag{2}$$

where $A$ is constant, $C$ is the content of the refractory elements in the $\gamma$ matrix phase. Therefore if the more amount of refractory elements W, Mo, Cr and Co are dissolved in the $\gamma$ matrix phase [27], the $\gamma$ matrix phase in the alloy will possess a better creep resistance according to Eq. (2).

The $\gamma'$ phase with $Ll_2$ structure in the alloy is the main strengthening phase, which may effectively hinder the dislocations motion. Since the deformation mechanism of the alloy during initial and steady state stages of creep is dislocations slipping in the $\gamma$ matrix phase, the high alloying degree of the $\gamma$ phase by refractory elements is critical to increase the resistance to dislocation movement, and hence to improve the creep resistance of the alloy. The resistance of the stress field producing between the adjacent dislocation lines may be expressed as follows [28].

$$\boldsymbol{\tau}_{\mathrm{dis}} = \frac{\mu \times \mathbf{b}}{8\pi(1-\upsilon)h} \tag{3}$$

where $\mu$ is the shear modulus, $\mathbf{b}$ is the Burgers vector, $h$ is the distance between two edge dislocations, $\upsilon$ is the Poisson ratio. It is indicated from Eq. (3) that the resistance of dislocations motion increases as the distance between the dislocation lines diminishes. Because the denser dislocations are activated in the $\gamma$ matrix channels, as shown in Fig. 4, the strain strengthening effect of the denser dislocations increases the resistance of the dislocations moving in the $\gamma$ matrix, which may decrease the strain rate of the alloy to result in the creep of alloy entering the steady state stage, as shown in Fig. 2.

### 4.2. Analysis on cracks initiated and propagated along boundaries

During the creep of polycrystalline nickel-based superalloy, the micro-cracks are firstly initiated along the boundaries vertical to the stress axis [29], as the creep goes on, the cracks gradually propagated along the grain boundaries until the creep fracture of the alloy, which indicates that the boundary is the weak region of the creep strength in alloy during creep. Although the boundary vertical to the stress axis in the DZ125 nickel-based superalloy has been eliminated by directional solidification technique, some upright and inclined boundaries relative to the stress axis exist still in the inter-dendrite regions, as shown in Fig. 1(b). Compared to $\gamma'$ and $\gamma$ phases, the boundaries are still the weaker region of the strength in the DS superalloy during creep, so that the initiation and propagation of cracks occur easily in the regions along boundaries, as shown in Fig. 7. But the upright boundary parallel to the stress axis and inclined boundary relative to the stress axis appear in the different regions of superalloy, and therefore, the initiation and propagation of the crack with various features occurs in the different regions, which is attributed to the boundaries bearing the different stress states.

It is understood that during the constant load creep, the maximum shearing stress in the specimen distributed in the direction of 45° angles relative to the stress axis, and the damage of alloy along boundaries is related to the maximum one during creep. And it is a reasonable consideration that the projection of the maximum shearing stress along the boundaries is the effective shearing stress which is responsible for initiating and propagating of the crack along the ones. During the constant load creep, the upright boundary parallel to the stress axis bears a smaller effective shearing stress, therefore, a few cracks initiated along the boundary. But the maximum effective shearing stress applies in the boundary at 45° angles relative to the stress axis, so that much more cracks initiated and propagated along the boundaries at 45° angles relative to the stress axis, as shown in Fig. 7.

The schematic diagrams of the crack initiating and propagating along the grain boundaries are indicated in Fig. 8, the direction of the applied stress is marked by the arrows, and the boundaries in alloy marked by the thicker lines. The schematic diagram of the upright boundary parallel to the stress axis is marked by the thicker line in Fig. 8(a). Since the upright one supports the smaller effective shearing stress, a few crack initiated along the one. However the crack easily initiated along the boundary at 45° angles relative to the stress axis due to the one supporting the maximum shearing stress, as shown in Fig. 8 (b). The direction of the effective shearing stress is marked by the fine long arrows, and the fine crack initiated in the boundary region, as marked by the short arrow. As the creep goes on, the propagation of the crack occurs along the boundary under the action of the maximum effective shearing stress, as shown in Fig. 8(c). This analysis is well agreement with the observation result, as shown in Fig. 7.

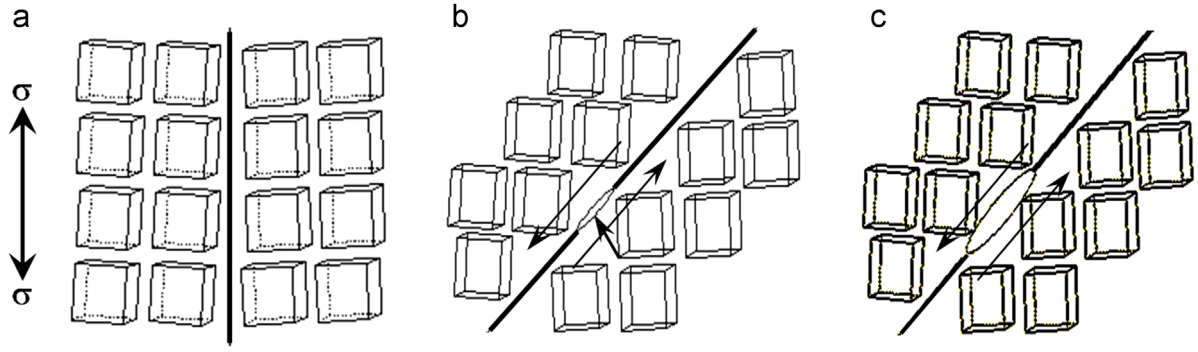


Fig. 8. Schematic diagrams of the cracks initiated and propagated along boundaries. (a) Upright boundaries, (b) crack initiated along inclined boundary, (c) propagation of crack.

## 5. Conclusions

(1) The microstructure of DZ125 alloy with full heat treatment consists of the cuboidal $\gamma'$ phase embedded coherently in $\gamma$ matrix, and the grain boundaries located in between the primary dendrite arm. The fine cuboidal $\gamma'$ phase dispersedly distributed in the dendrite arm regions, and the coarser cuboidal $\gamma'$ phase distributed in the inter-dendrite regions; an obvious un-homogeneity of the $\gamma'$ phase in size occurs in between the dendrite and inter-dendrite regions.

(2) In the primary creep stage, the cubical $\gamma'$ phase in the alloy transformed into the rafted structure along the direction vertical to the stress axis, and dislocations slipping in the $\gamma$ matrix and climbing over the rafted $\gamma'$ phase are the deformation mechanism of the alloy during steady-state creep.

(3) In the latter stage of creep, the deformation mechanism of the alloy is dislocations slipping in the $\gamma$ matrix, and $\langle 1\ 1\ 0\rangle$ super-dislocation shears into the rafted $\gamma'$ phase for slipping on $\{1\ 1\ 1\}$ planes. The creep damage of the alloy includes in the initiation and propagation of the micro-cracks along boundaries, and the various damage features display in the boundary regions with different configurations.

(4) The boundaries about at 45° angles relative to the stress axis support the bigger effective shear stress, which increases the damage probability during creep. However, the adding Hf element may promote the precipitation of the fine carbides along boundaries to restrain the dislocation slipping for improving the creep resistance. This is considered to be the main reason of the boundaries displaying the non-smooth surfaces after creep rupture of the alloy.

## References

[1] W.H. Jiang, H.R. Guang, Z.Q. Hu, Mater. Sci. Eng., A 217 (1999) 101–108.
[2] Y.Z. Zhou, A. Volek, R.F. Singer, Metall. Mater. Trans. A 36 (2005) 651–656.
[3] W.G. Zhang, L. Liu, X.B. Zhao, M. Qu, Z.H. Yu, H.Z. Fu, Foundry 58 (2009) 1–6.
[4] L.Y. Sheng, F. Yang, T.F. Xi, C. Lai, J.T. Guo, Mater. Res. Innovations 17 (2013) 101–106.
[5] S.J. Moss, G.A. Webster, E. Fleury, Metall. Mater. Trans. A 27 (1996) 829–837.
[6] A. Dlouhý, R. Schäublin, G. Eggeler, Scr. Mater. 39 (1998) 1325–1332.
[7] J.X. Zhang, J.C. Wang, H Harada, Y. Koizumi, Acta Mater. 53 (2005) 4623–4633.
[8] J.M. Cairney, T.S. Rong, I.P. Jones, R.E. Smallman, Philos. Mag. 83 (2003) 1827–1843.
[9] L. Shui, T. Jin, S.G. Tian, Z. Hu, Mater. Sci. Eng., A 454 (2007) 461–466.
[10] M. Feller-Kniepmeier, T. Kuttner, Acta Metall. Mater. 42 (1994) 3167–3174.
[11] A.C. Picasso, A.J. Marzocca, I. Alvarez, Mater. Sci. Eng., A 234 (1997) 1099–1102.
[12] W.J. Harrison, M.T. Whittaker, C. Deen, Mater. Res. Innovations 17.5 (2013) 323–326.
[13] J.T. Guo, Acta Metall. Sinica 14.11 (2005) 1221–1227.
[14] C. Wang, J. Zhang, L. Liu, H. Fu, J. Alloys Compd. 508.2 (2010) 440–445.
[15] C. Mayr, G. Eggeler, A. Dlouby, Mater. Sci. Eng., A 207.1 (1996) 51–63.
[16] S.G. Tian, Y. Su, B.J. Qian, X.F. Yu, F.S. Liang, A.N. Li, Mater. Des. 37 (2012) 236–242.
[17] L. Shui, T. Jin, S.G. Tian, Z.Q. Hu, Mater. Sci. Eng., A 454 (2007) 461–466.
[18] S.G Tian, J.H. Zhang, H.H. Zhou, H.C. Yang, Y.B. Xu, Z.Q. Hu, Mater. Sci. Eng., A 262 (1999) 271–278.
[19] S.G Tian, J.H. Zhang, H.H. Zhou, H.C. Yang, Y.B. Xu, Z.Q. Hu, Mater. Sci. Technol. 14 (1998) 751–756.
[20] R. Lagneborg, B. Bergman, Met. Sci. 10.1 (1976) 20–28.
[21] S.G. Tian, H.H. Zhou, J.H. Zhang, H.C. Yang, Y.B. Xu, Z.Q. Hu, Mater. Sci. Eng., A 279 (2000) 160–165.
[22] S.G. Tian, X. Ding, Z.G. Guo, J. Xie, Y.C. Xue, D.L. Shu, Mater. Sci. Eng., A 594 (2014) 7–16.
[23] E.I. Meletis, K. Lian, J. Mech. Behav. Mater. 6.1 (1995) 69–84.
[24] Y.W. Fang, Y.H. Li, J. Mater. Eng. Perform. 22.6 (2013) 1565–1573.
[25] B. Tomkins, Philos. Mag. 18.155 (1968) 1041–1066.
[26] R.L. Fleischer, Acta Metall. 11.3 (1963) 203–209.
[27] W.T. Loomis, J.W. Freeman, D.L. Sponseller, Metall. Trans. 3.4 (1972) 989–1000.
[28] T.M. Pollock, A.S. Argon, Acta Metall. Mater. 40.1 (1992) 1–30.
[29] J. Xie, S.G. Tian, X.M. Zhou, X.F. Yu, W.X. Wang, Mater. Sci. Eng., A 538 (2012) 306–314.